# Mechanisms and Modeling of Cleavage Fracture in Simulated Heat-Affected Zone Microstructures of a High-Strength Low Alloy Steel

A. LAMBERT-PERLADE, A.F. GOURGUES, J. BESSON, T. STUREL, and A. PINEAU

The effect of the welding cycle on the fracture toughness properties of high-strength low alloy (HSLA) steels is examined by means of thermal simulation of heat-affected zone (HAZ) microstructures. Tensile tests on notched bars and fracture toughness tests at various temperatures are performed together with fracture surface observations and cross-sectional analyses. The influence of martensite-austenite (M-A) constituents and of "crystallographic" bainite packets on cleavage fracture micromechanisms is, thus, evidenced as a function of temperature. Three weakest-link probabilistic models (the "Master-curve" (MC) approach, the Beremin model, and a "double-barrier" (DB) model) are applied to account for the ductile-to-brittle transition (DBT) fracture toughness curve. Some analogy, but also differences, are found between the MC approach and the Beremin model. The DB model, having nonfitted, physically based scatter parameters, is applied to the martensite-containing HAZ microstructures and gives promising results.

## I. INTRODUCTION

HIGH-STRENGTH low alloy (HSLA) steels are now widely used for structural applications. These materials combine excellent tensile strength and ductile-to-brittle transition (DBT) properties. However, this combination of high strength and high fracture toughness can be deteriorated after welding thermal cycles. The degradation of the fracture toughness of HSLA steels after welding is attributed to the formation of "local brittle zones" in the welded joint.[1,2] Significant embrittlement can be encountered in the coarse-grained heat-affected zone (CGHAZ) and, in particular, in the intercritically reheated CGHAZ (ICCGHAZ) of multipass welded joints (*e.g.*, References 3 through 7).

According to literature data, the fracture toughness of these local brittle zones is influenced by metallurgical factors such as prior austenite grain size, bainite packet size, and distribution of second phases such as carbides and martensite-austenite (M-A) constituents (*e.g.*, References 5 and 8 through 10). The cleavage-facet size has been related to the prior austenite grain size.[9] The bainite packet boundary influences the brittle fracture properties of the heat-affected zone (HAZ) in a HY-80 grade steel[11] as well as in other bainitic steels (*e.g.*, References 12 through 15). On the other hand, M-A constituents have a deleterious effect on both crack initiation and propagation (*e.g.*, References 2, 8 through 10, 16, and 17). However, correlation between welding thermal cycles, the resulting microstructures, and fracture toughness properties has only been scarcely evidenced in detail yet. Better understanding of the fracture micromechanisms operating in these complex microstructures is still needed, which is the aim of the present study.

A. LAMBERT-PERLADE and T. STUREL, Research Engineers, are with Arcelor Research & Development, IRSID, 57283 Maizières-lès-Metz cedex, France. A.F. GOURGUES, Lecturer, J. BESSON, Researcher, and A. PINEAU, Professor, are with the Centre des Matériaux, Ecole des Mines de Paris, UMR CNRS 7633 91003 Evry cedex, France. Contact e-mail: anne-francoise.gourgues@mat.ensmp.fr

Manuscript submitted June 5, 2003.

The purpose of this work is to investigate cleavage fracture micromechanisms of HAZ microstructures in order to determine and to model the effect of local brittle zones on fracture toughness of a HSLA steel weld. To avoid experimental difficulties that could arise due to the heterogeneous nature of the HAZ in a welded joint, a thermal-simulation technique was chosen to obtain homogeneous microstructures in "macroscopic" specimens. Cleavage fracture micromechanisms were studied with smooth and round-notched (RN) tensile bars, acoustic-emission (AE) monitoring of cleavage cracking, and subsequent metallographic analysis. The results were used to model crack initiation near a M-A constituent and crack propagation in the bainitic matrix. Following a local approach to fracture, models based on the study of these fracture micromechanisms were then used to account for the effect of microstructure and test temperature on fracture toughness properties.

## II. MATERIAL AND EXPERIMENTAL PROCEDURES

### A. *Materials and Microstructures*

The HSLA steel used in the present study was provided as a 40-mm-thick plate obtained after thermal-mechanical–controlled processing. Its chemical composition is 0.07C-1.5Mn-0.32Si-0.47Ni-0.12Mo-0.16Cu-0.06Cr-0.03Al-0.014Nb-0.012P-0.001S-0.006N (wt pct). The plate exhibits a ferrite-pearlite microstructure with a mean ferrite grain size of 5 $\mu$m (Figure 1(a)). At room temperature, the yield strength and ultimate tensile strength are 433 and 534 MPa, respectively. This microstructure will be referred to as the "base metal" microstructure.

To simulate the CGHAZ and ICCGHAZ microstructures, heat treatments consisting of, respectively, one and two thermal cycles were chosen. They were applied to blanks cut from the midthickness of the plate along the transverse direction of the base metal. A Gleeble 1500 thermal-mechanical simulator (Dynàmic Systems Inc., Poestenkill, NY) was used to apply the thermal cycles with a heating rate of 520 °C · $s^{-1}$. The maximum temperature of the first cycle was $Tp_1 = 1250$ °C. Cooling times from 800 °C to 500 °C ($\Delta t^{8/5}$) were chosen to

be 25 seconds (CGHAZ-25 microstructure) and 120 seconds (CGHAZ-120 microstructure), corresponding to a medium and high heat-input welding energy, respectively. Intercritical reheating of the CGHAZ-25 microstructure at maximum temperature ($Tp_2 = 775$ °C), with the same cooling conditions as CGHAZ-25, induced partial austenitization of the bainitic GCHAZ-25 microstructure. The resulting intercritically reheated microstructure will be referred to as the ICCGHAZ-25 microstructure. Upon further cooling, austenite was partially transformed into martensite, leading to the formation of M-A constituents. Heat treatments and metallurgical properties of simulated HAZ microstructures are summarized in Table I. The resulting tensile and conventional Charpy V-notch impact toughness properties are shown in Table II.

Simulated HAZ microstructures mainly consist of upper bainite (Figure 1), whose microstructure is controlled by the first thermal cycle conditions. Due to the lower cooling rate, CGHAZ-120 has a slightly higher prior austenite grain size and a granular bainitic matrix. The bainite packets were defined as crystallographic units delimited by high-angle boundaries. Their size distribution was measured using electron backscatter diffraction (EBSD) maps of metallographic sections (Figure 2 and Table I). As a consequence of bainitic quenching, HAZ microstructures are generally stronger than the base metal (Figure 3), but the low-temperature ($T \leq -150$ °C) ductility of simulated HAZ materials is much lower than that of the base metal.

Carbides and M-A constituents, resulting from the incomplete transformation of austenite into bainite during cooling, are present in all HAZ microstructures. The ICCGHAZ-25 contained a significantly higher volume fraction of M-A constituents (Table I), which were larger and more numerous than in the other HAZ microstructures (Figure 2). More details about M-A constituents in these microstructures can be found elsewhere.[18,19] Here, it is enough to say that the large, "blocky" M-A particles often consist of carbon-enriched martensite islands surrounded by a thin, noncontinuous austenite film. They are often located at the former austenite grain boundaries. Elongated M-A particles, located between the bainite laths, were found using transmission electron microscopy to be mostly austenitic. All M-A particles are rich in carbon (1.0 to 1.4 wt pct). Only 10 pct of the retained austenite further transforms into martensite upon cooling to −196 °C.

### B. *Experimental Procedures*

The effect of microstructure on fracture toughness properties was investigated using fatigue-precracked three-point bend (TPB) $10 \times 20 \times 100$ mm$^3$ specimens (ligament size of 10 mm). The specimens were fatigue precracked using a maximum load level lower than 4500 N and a load ratio of 0.1. The number of cycles used in the precracking procedure was about $4.5 \times 10^5$. The specimens were cut in the midthickness of the plate, along the transverse direction, with the crack propagating along the rolling direction. Calculation of the J integral was carried out using the area under the load-load line displacement curve following ASTM standard E1820-01.[20] The $J_{Ic}$ values were converted into a stress intensity factor ($K_J$) by assuming plane-strain conditions: $K_J = (E \cdot J_{Ic})^{1/2} \cdot (1 - \nu^2)^{-1/2}$, where $\nu$ is the Poisson ratio and $E$ is the Young's modulus of the material. In this study, the upper-limit criterion for $J_{Ic}$ ($J > (W - a) \cdot \sigma_y/M$, with $(W - a)$ being the ligament size) was calculated with both $M = 30$ (used in the Master-curve (MC) approach), $M = 50$, and $M = 100$.[20]

Cleavage fracture micromechanisms were investigated using RN specimens over a wide temperature range (−196 °C to room temperature). The effect of stress triaxiality was studied using various notch radii (5, 2, 1, or 0.1 mm) with a minimum diameter ($Ø_0$) of 5 mm and outer diameter of 9 mm. The corresponding specimens are referred to as RN5, RN2, RN1, and RN0.1, respectively. The local stress triaxiality ratio ($\tau$) is defined as follows: $\tau = \sigma_m/\sigma_{eq}$, where $\sigma_m$ is the local hydrostatic stress and $\sigma_{eq}$ is the local Von Mises equivalent stress. Typical mean (maximum) values of $\tau$ over the area of

**Table I. Heat Treatment and Metallurgical Features of the Simulated HAZ Microstructures**

| | Heat Treatment | | | Mean Size ($\mu$m) | | | |
|---|---|---|---|---|---|---|---|
| Microstructure | $T_{p1}$ (°C) | $T_{p2}$ (°C) | $\Delta t^{8/5}$ (s) | Former $\gamma$ Grains | Bainite Packets (EBSD) | Area Fraction of Second Phases (Optical Microscopy, in Pct) | Pct Retained Austenite (X-Ray Diffraction) |
| CGHAZ-25 | 1250 | — | 25 | 56 | 12 | 4 | 2 |
| ICCGHAZ-25 | 1250 | 775 | 25 | 60 | 12 | 8 | 4 |
| CGHAZ-120 | 1250 | — | 120 | 76 | 35 | 5 | 4 |

**Table II. Impact Toughness and Room-Temperature Properties of the Investigated Microstructures (Midthickness, Transverse Direction)***

| Microstructure | $HV_{10}$ | YS (MPa) | TS (MPa) | Fracture Elongation (Pct) | Reduction in Area (Pct) | $n$ | YS/TS | $T_{70J}$ (°C) |
|---|---|---|---|---|---|---|---|---|
| Base metal | 168 | 433 | 534 | 22 | 77 | 0.19 | 0.81 | −89 |
| CGHAZ-25 | 225 | 580 | 690 | 23 | 79 | 0.08 | 0.84 | −31 |
| ICCGHAZ-25 | 203 | 475 | 680 | 26 | 73 | 0.12 | 0.70 | +11 |
| CGHAZ-120 | 184 | 476 | 625 | 25 | 79 | 0.14 | 0.76 | +15 |

*HV is the Vickers hardness, YS the yield strength, TS the tensile strength, $n$ the strain hardening exponent, and $T_{70J}$ the temperature for which the mean Charpy V-notch impact energy is 70 J.

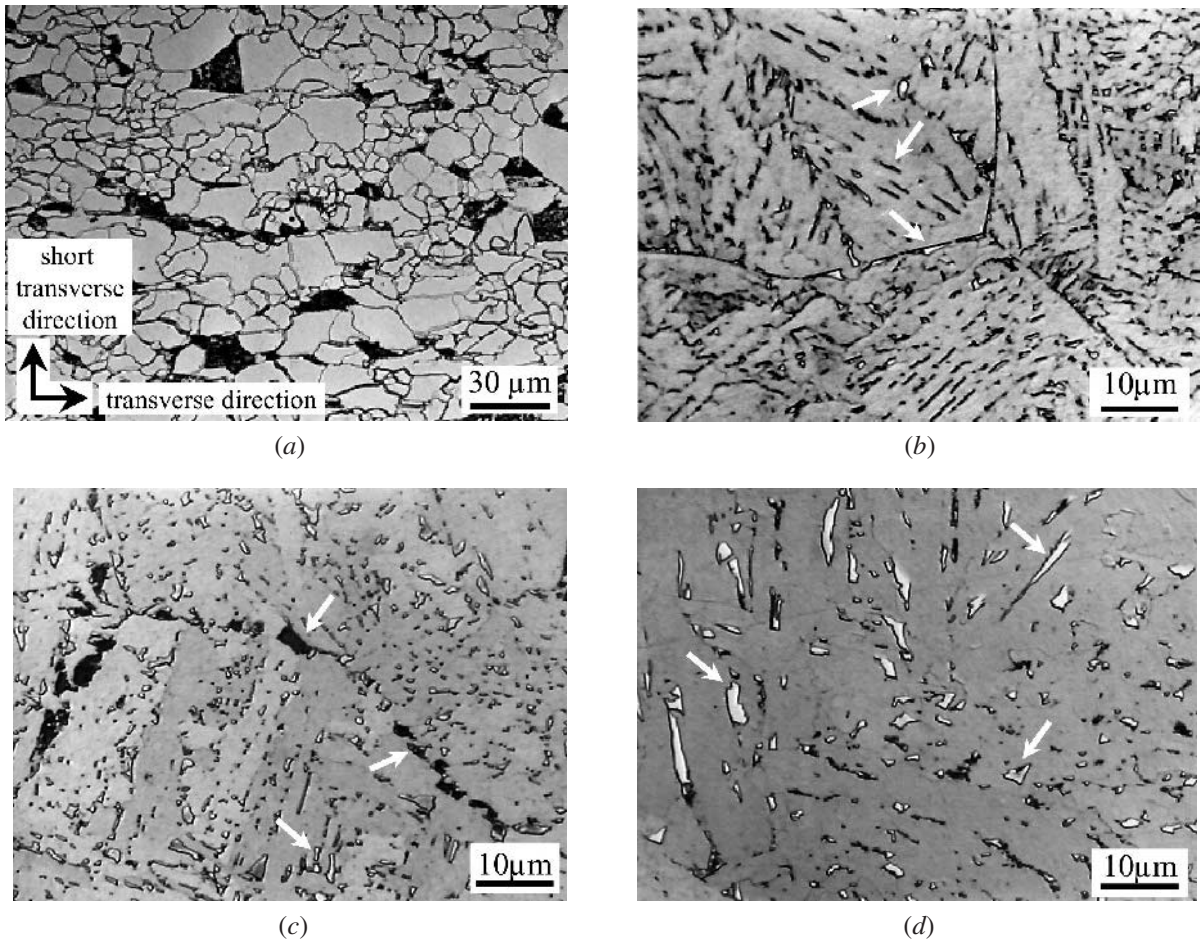


Fig. 1—Light optical micrographs of the base metal (midthickness, nital etching) and simulated heat-affected zone (1 pct sodium bisulphite etching) microstructures: (*a*) base metal, (*b*) CGHAZ-25, (*c*) ICCGHAZ-25, and (*d*) CGHAZ-120. Some M-A constituents are indicated by white arrows.

minimum section were calculated to be 0.6 (maximum of 0.7), 0.8 (maximum of 1.0), 1.1 (maximum of 1.3), and 1.4 (maximum of 1.7) for the RN5, RN2, RN1, and RN0.1 specimens, respectively.

Some of the tests with both the TPB and RN0.1 specimens (between −60 °C and +20 °C) were run together with AE monitoring in order to investigate cleavage crack events. More details are reported in Reference 21 and in the Appendix. The AE technique allowed detection of any microcracking event as highly energetic peaks, and, thus, investigation of whether final fracture was preceded by nucleation and propagation of microcracks. Fracture was considered to be controlled by crack propagation, as long as (at least) one microcrack event could be detected before final fracture of the specimen. At very low temperatures, no microcrack event could be detected, so that fracture was considered to be nucleation controlled. The AE technique also allowed interruption of the test after the detection of microcracking, but still before final fracture. After test interruption, the RN0.1 specimens containing cleavage cracks were machined to smooth bars (minimum diameter of 4.8 mm). Both "interrupted" TPB specimens and specimens machined from RN0.1 tested bars were then fatigue fractured. In all cases, the fatigue crack initiated from arrested cleavage microcracks, which could, thus, be easily detected and studied on the fracture surfaces.

### C. *Numerical Procedures*

A local approach to cleavage fracture consists of applying a physically based fracture criterion at every location of a loaded component, in order to derive a failure criterion for this component using a weakest-link assumption.[22,23] This requires the knowledge of the local stress and strain fields at any point in the component. The stress and strain fields were determined using a finite-element (FE) method for all specimen-geometry and test conditions with the finite deformation formalism, updated geometry, and a global convergence criterion. Quadratic elements (eight nodes) with reduced integration (four Gauss points per element) were used for all calculations, and the Young's modulus and Poisson ratio were taken to be 210 GPa and 0.3, respectively.

All materials were assumed to follow the Von Mises yield criterion. Elastic-plastic constitutive equations were thoroughly determined as a function of test temperature for all microstructures using the tensile properties determined with smooth specimens (gage length as small as 10 mm for the simulated HAZ microstructures). For the base metal, a power-law hardening equation was found to best represent the tensile properties. For the simulated HAZ microstructure, a nonlinear isotropic hardening rule was chosen with two hardening variables, as given by the following equation in the uniaxial case:

$$\sigma = R_0 + Q_1(1 - \exp(-b_1 \cdot p)) + Q_2(1 - \exp(-b_2 \cdot p)) \quad [1]$$

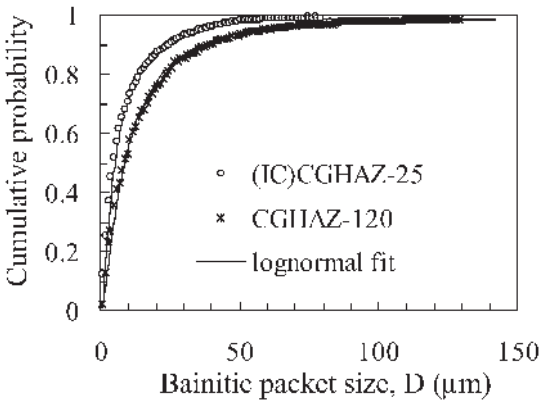


(*a*)

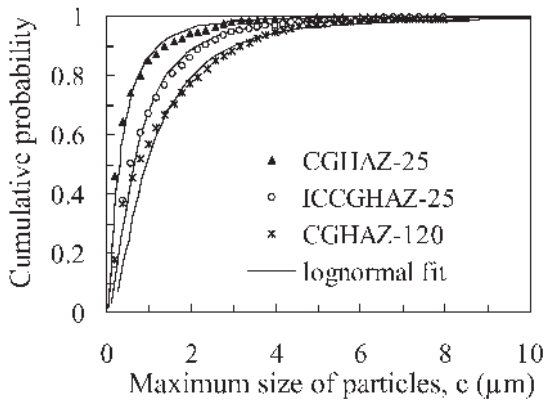


(*b*)

Fig. 2—Size distribution of (*a*) bainitic packets and (*b*) second-phase particles in the simulated HAZ microstructures.

In Eq. [1], the parameters $R_0$, $Q_1$, $Q_2$, $b_1$, and $b_2$ depend on both the material and test temperature, and $p$ is the cumulative plastic strain. The constitutive equations had to be slightly modified (reduction of the $R_0$ parameter by about 5 pct) to accurately represent the load-load line displacement curves of RN specimens. This is due to a pseudo-Lüders plateau observed in the tensile stress-strain curves. More details concerning the fitting procedure can be found elsewhere.[19]

For RN specimens, the stress and strain fields were computed in axisymmetrical conditions using the constitutive equations determined previously and a minimum mesh size of 200 $\mu$m. For each temperature, material, and specimen-geometry condition, the load was applied by displacement control remote from the gage area. The mean stress ($\sigma_{mean}$, *i.e.*, the calculated macroscopic load divided by the updated area of minimum diameter) and mean radial strain ($\varepsilon_{mean} = 2 \cdot \ln(\text{Ø}_0/\text{Ø})$, with Ø being the calculated minimum diameter, having an initial value $\text{Ø}_0$) were then calculated and compared with experimental data. Excellent agreement was obtained between experimental and simulated $\sigma_{mean}$ *vs* $\varepsilon_{mean}$ curves.

For TPB specimens, the load–crack mouth displacement curves fall between those calculated assuming plane-stress and plane-strain conditions, respectively. Thus, only a three-dimensional (3-D) mesh could allow accurate prediction of the load–crack mouth displacement curve. This was confirmed by carrying out calculation in 3-D conditions for one microstructure and test temperature. Due to the small specimen thickness (10 mm), the stress state at the crack tip is close to plane-stress conditions near the side free surfaces. However, for the low values of fracture toughness considered in the present study, it remains close to plane-strain conditions in the major part of the crack front. Thus, to speed up calculations for all microstructures and test temperatures, plane-strain conditions were assumed to compute local stress and strain fields near the crack. To accurately describe the stress and strain fields near the crack, an initial crack blunting of 3 $\mu$m (*i.e.*, one-sixth of the expected crack tip opening displacement) was modeled in the mesh, following the approach reported by McMeeking.[24] Thus, the mesh size very near the crack tip was lower than 1 $\mu$m. The initial mesh size in the area of maximum stress was about 20 $\mu$m. The specimen was loaded by controlling the displacement of elastic loading pins. The contact conditions (here, mixed sliding and friction) were shown to have no influence on the results of the local approach, at least in the brittle temperature range considered in the present study.

## III. EXPERIMENTAL RESULTS AND DISCUSSION

### A. *Mechanical and Macroscopic Fracture Properties*

#### 1. *Smooth and round-notched specimens*

The DBT properties of RN specimens are shown in Figure 4 for the RN2 specimen geometry. The mean fracture strain ($\varepsilon_R$) was evaluated as the value of $\varepsilon_{mean}$ for which macroscopic cracking started, *i.e.*, corresponding to an abrupt change in the slope of the load-load line displacement curve. As shown in Figure 4, welding thermal cycles have a deleterious effect on the transition temperature. They also affect both the lower- and upper-shelf values of $\varepsilon_R$ in the transition curve.

#### 2. *Fracture mechanics specimens*

The DBT curves obtained with the TPB specimens are shown in Figure 5. Thermal cycles markedly decrease the toughness of the investigated steel (Table II). The transition temperature increases with both the bainite packet size (CGHAZ-25 *vs* CGHAZ-120) and the volume fraction of M-A constituents for a given bainite packet size (CGHAZ-25 *vs* ICCGHAZ-25). Whatever the microstructure, and due to stress triaxiality effects, the DBT temperature is much higher for the fracture mechanics specimens than for the RN2 specimens (compare Figure 5 with Figure 4).

### B. *Fracture Micromechanisms*

Damage mechanisms were investigated by observing fracture surfaces and polished cross sections of the tested specimens. As will be shown subsequently, fracture micromechanisms and relevant microstructural parameters are the same for the smooth, RN, and fracture mechanics specimens. As expected from the higher stress triaxiality ratio ($\tau$) of about 3, the DBT temperature is higher for fracture mechanics specimens than for notched specimens. The higher scatter observed with fracture mechanics specimens could be due to either the intrinsic scatter associated with brittle fracture, or to sampling effects: in fracture mechanics specimens, only a small volume of the material is sampled by the stress field ahead of the crack tip.

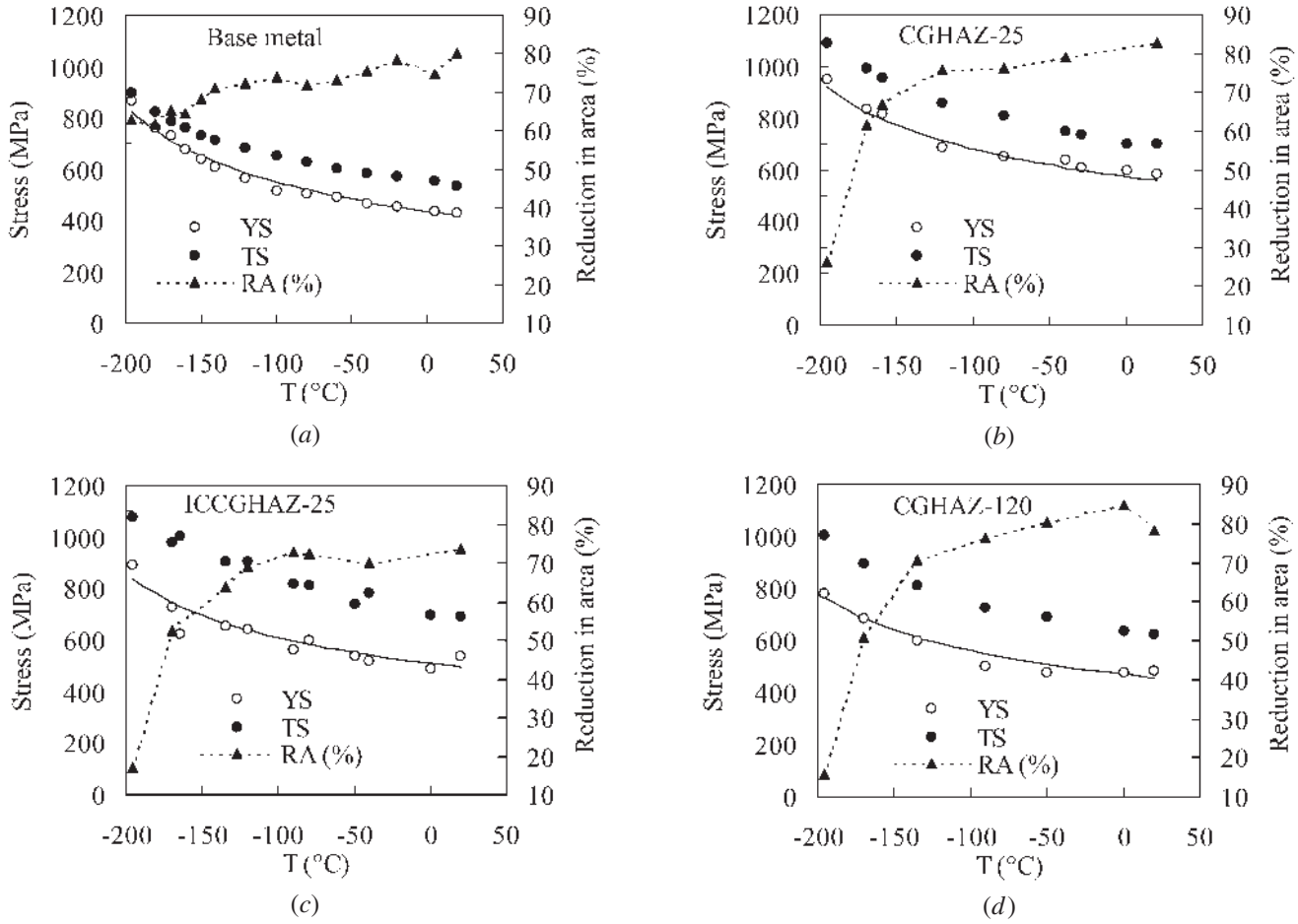


Fig. 3—Temperature dependence of yield strength (YS), tensile strength (TS), and reduction in area (RA) of (*a*) base metal, (*b*) CGHAZ-25, (*c*) ICCGHAZ-25, and (*d*) CGHAZ-120 microstructures. Solid lines are for the (YS *vs* temperature) fit used in the constitutive equations.

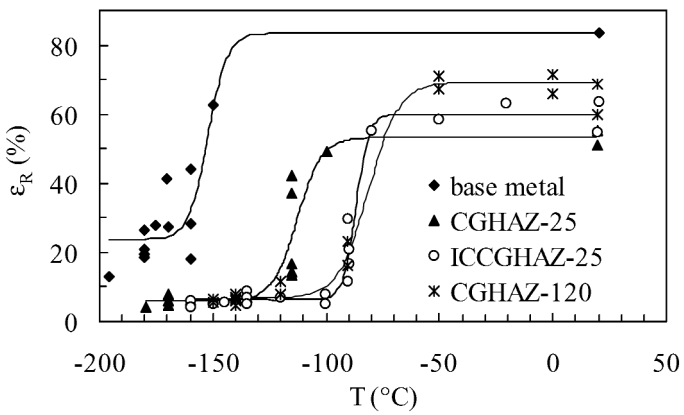


Fig. 4—Brittle to ductile transition curve of RN2 specimens, evaluated using the mean fracture strain $\varepsilon_R$.

1. *Effect of temperature on fracture properties*

Fully ductile, dimpled fracture surfaces were observed in the ductile temperature range. In the brittle temperature range, fracture occurred by cleavage only. No damage was detected by cross-sectional examination of specimens fractured in the lowest temperature range ($T \leq -170$ °C), suggesting that at very low temperatures, cleavage might be controlled by crack initiation.

In the transition temperature range, cleavage cracking occurred after some ductile damage. Interrupted tests showed that in RN specimens, crack initiation always occurred where the calculated principal stress was maximal, *i.e.*, either in the bulk or near the notch root, depending on specimen geometry. In fracture mechanics specimens, the amount of damage observed underneath the fracture surface increases with test temperature, and for higher values of $K_{Jc}$, stable ductile crack propagation was followed by final cleavage fracture (open symbols in Figure 5). The number of cracking events detected before final fracture increases with test temperature. Using AE monitoring, microcrack initiation and arrest were detected for values of $K_J$ higher than 30 to 40 MPa$\sqrt{m}$ for all investigated test temperatures. Interrupted tests showed that cleavage crack initiation occurs ahead of the front of the fatigue precrack (Figure 6). Due to multiple-site crack initiation, the values of the distance between the first cleavage microcracks and the fatigue precrack, which were measured after interrupted tests, did not allow an estimation of the local fracture stress. For fracture strain values of at least a few percentages, numerous arrested cleavage microcracks were found near the fracture surface, indicating that cleavage cracking was controlled by crack propagation. This was confirmed by the presence of multiple cleavage crack initiation sites in the fracture surfaces obtained after interrupted tests.

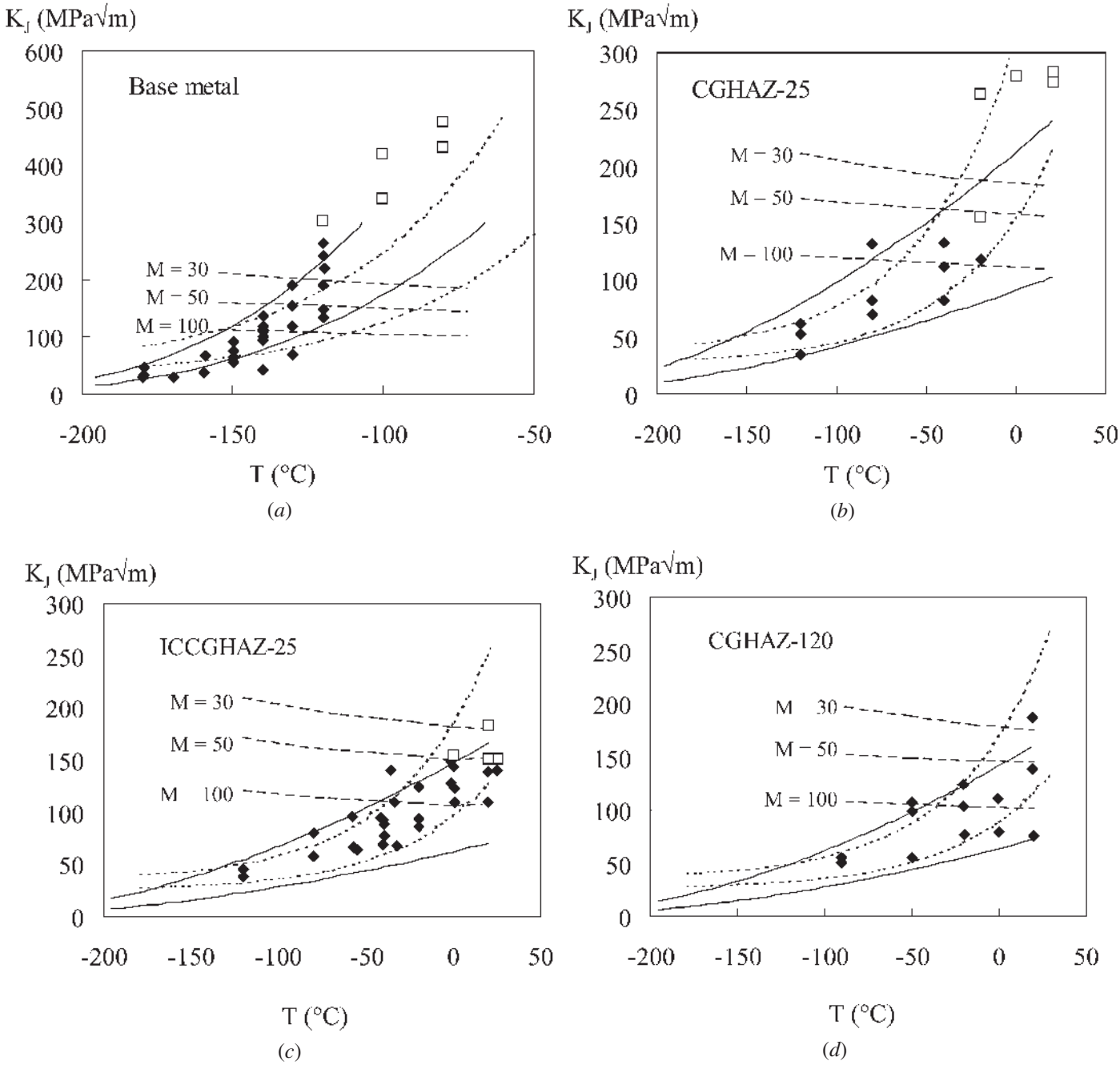


Fig. 5—Brittle to ductile toughness transition curves obtained with TPB specimens: (*a*) base metal, (*b*) CGHAZ-25, (*c*) ICCGHAZ-25, and (*d*) CGHAZ-120 microstructures. Open symbols indicate that significant (>0.2 mm) ductile crack propagation occurred before cleavage fracture. Solid lines (respectively, dotted lines) show fracture probabilities of 10 and 90 pct given by the Beremin model (respectively, by the "Master curve" approach). Dashed lines indicate the upper limit for calculation of the $K_J$ parameter ($J > (W - a) \cdot \sigma_y/M$), with $(W - a)$ the ligament size (10 mm).

2. *Cleavage crack initiation micromechanisms at temperatures higher than −170 °C*

In the ductile temperature range, the largest ductile dimples initiated from small CaS, or from Ca-rich or Al-rich, oxide inclusions. The smallest ductile dimples were found to initiate from M-A constituents, as revealed from Villela etching of fracture surfaces (Figure 7(a)). At lower temperatures, cleavage initiates near M-A particles (Figure 7(b)). Many secondary cleavage cracks were also associated with M-A particles, confirming the key role of M-A particles in brittle cleavage fracture of simulated HAZ microstructures.

Tests on smooth and on notched specimens showed that the effect of M-A particle morphology depends on both test temperature, loading conditions, and aspect ratio of the particle. The nature of the particles (mostly austenite in elongated particles located between the bainite laths, mostly brittle martensite in more blocky particles)[18] plays a role at low strain (<5 pct) and low stress triaxiality only. Metallographic analyses of fractured specimens, as well as magnetic measurements on smooth tensile specimens strained by 5 pct both at 20 °C and at −196 °C, showed that for fracture strains higher than about 5 pct, or very near the fracture surface, or at very low temperatures, or

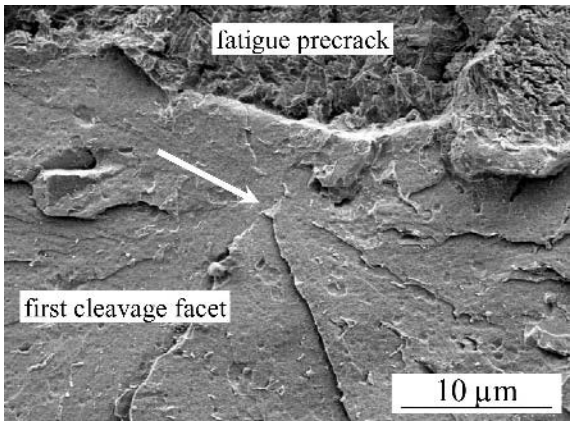


Fig. 6—Cleavage crack initiation observed after interrupted test of a fracture mechanics specimen; $T = 20$ °C, ICCGHAZ-25 microstructure. The cleavage crack initiated near a M-A constituent (arrow), as shown after Villela etching of the fracture surface.

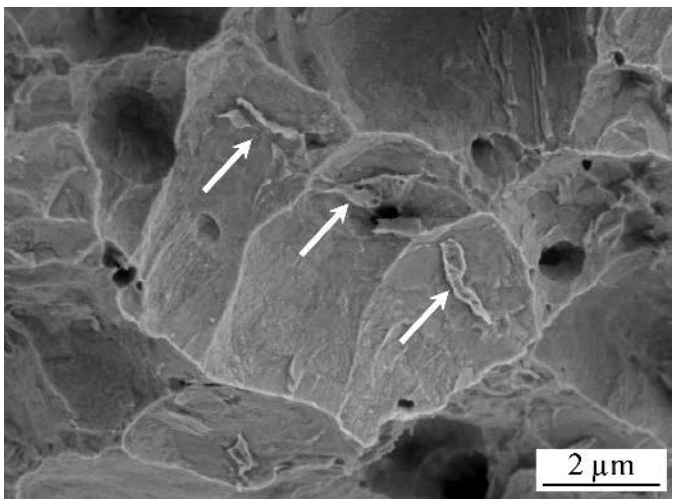


(*a*)

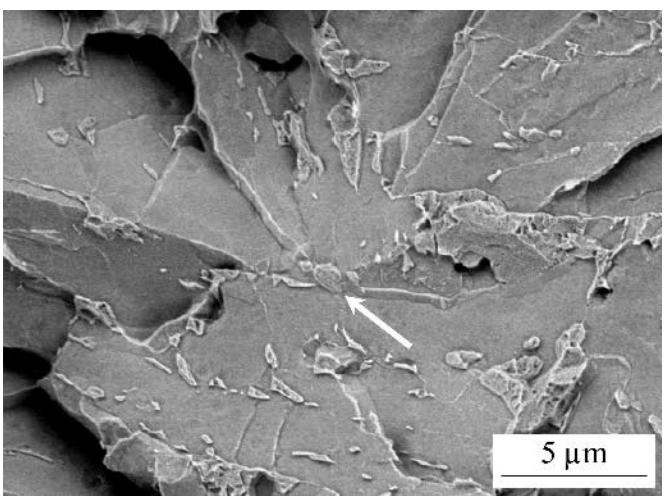


(*b*)

Fig. 7—Fracture surfaces of RN2 specimens (ICCGHAZ-25 microstructure). (*a*) Ductile fracture at $T = +20$ °C (fracture strain 53 pct). (*b*) Brittle cleavage fracture at $T = -160$ °C (fracture strain 4 pct). Both smallest ductile dimples and cleavage facets are found to initiate near M-A constituents, as indicated by arrows (Villela etching).

for a high stress triaxiality ratio (RN0.1 and TPB specimens), all M-A particles were transformed into martensite during the test and became brittle. Metallographic analyses showed that the most brittle particles are the most elongated ones along the macroscopic loading axis.

The damage micromechanism acting at the M-A constituents depends on the local stress triaxiality ratio. For low mean values of $\tau$ ($\tau_{\text{mean}} < 1.2$), *i.e.*, for smooth RN2 and RN1 specimens, damage initiated by interfacial decohesion between M-A particles and the surrounding bainitic matrix, most often appearing near the edges of the M-A particles. For higher values of $\tau$, *i.e.*, for the RN0.1 and TPB specimens, damage initiated by brittle fracture of the M-A constituents.

Competing effects between M-A/matrix interfacial decohesion and M-A particle cracking were accounted for using a micromechanical model, where the maximum principal stress $\sigma_{M\text{-}A}$ in the M-A particle was shown to be expressed by

$$\sigma_{M\text{-}A} = \sigma_1 + 1.8 \cdot (\sigma_{eq} - \sigma_y) \qquad [2]$$

where $\sigma_1$, $\sigma_{eq}$, and $\sigma_y$ refer to the local maximum principal stress, the local von Mises equivalent stress, and the yield stress of the bainite matrix, respectively. The value of 1.8 was adjusted using the results of unit-cell FE calculations of elastic martensite particles embedded in a bainitic matrix.[19] On the other hand, interfacial decohesion between the M-A particle and matrix near the particle edges was modeled by applying locally the classical ductile-fracture criterion developed by Rice and Tracey. These competing effects were then calculated in RN specimens by a post-processing procedure. The results showed that the local damage mechanism near M-A particles strongly depends on the stress triaxiality effects induced by specimen geometry, as observed experimentally. The critical (brittle) fracture stress in the M-A particle was fitted to be $\sigma^c_{M\text{-}A} \approx 2200$ MPa, in order to match the area where fracture of M-A constituents was, respectively, predicted by the model and observed experimentally in a cross section of tested RN specimens.[19]

3. *Cleavage microcrack arrest micromechanism*

Arrested cleavage microcracks were investigated after interrupted tests (Figure 8(a)). Crack arrest occurred at high-angle bainite packet boundaries, as shown by EBSD measurements on fracture surfaces (Figure 8(a)),[25] which are difficult in nature, and on polished cross sections (Figures 8(b) and (c)), which only provide in-plane information. Disorientation measurements as exemplified in Figures 8(a) and (c) suggest that the "crystallographic" bainite packet size (*i.e.*, the size of bainite entities delimited by high-angle boundaries, shown in Figure 2) is a relevant parameter to investigate crack propagation conditions.

The bainitic matrix plays a key role in cleavage crack propagation and arrest. The M-A particles are expected not to be significantly harmful as long as bainite packets are sufficiently small. Such a beneficial effect of a refined matrix microstructure has recently been reported for bainitic steels containing brittle TiN particles.[26] Concerning the simulated HAZ microstructures containing M-A constituents, this hypothesis was confirmed experimentally[19] by using a "refined bainite" simulated HAZ microstructure of the same steel as in the present study ($Tp_1 = 1200$ °C, cooling at 50 °C · $s^{-1}$ to 775 °C, kept at 775 °C for 2 seconds, then the same cooling conditions as for GCHAZ-25). Despite a high amount

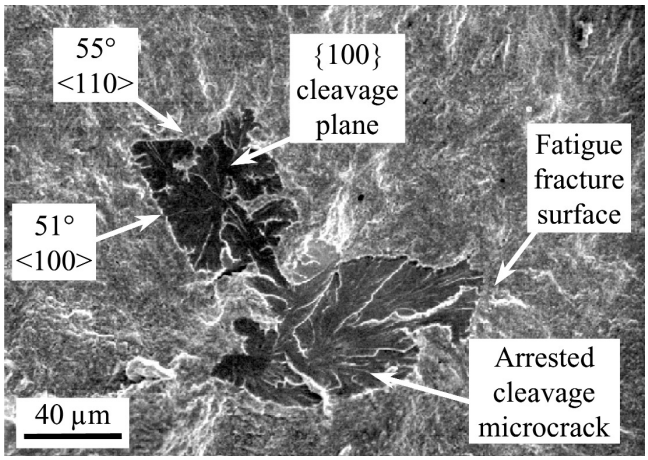


(*a*)

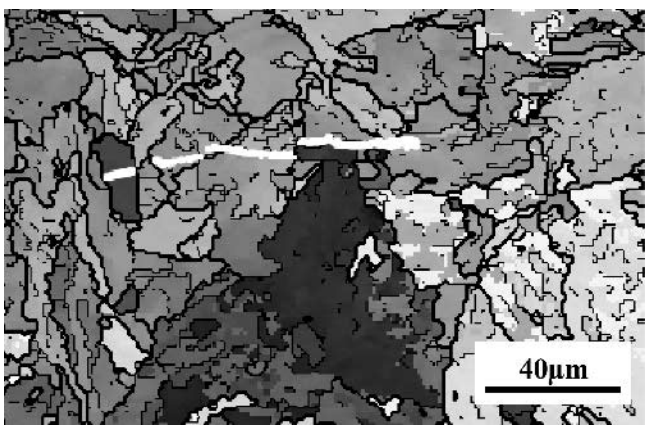


(*b*)

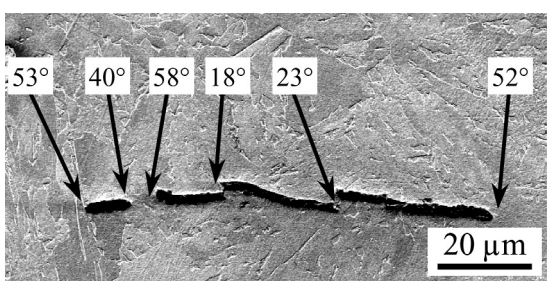


(*c*)

Fig. 8—Arrested cleavage microcracks obtained with interrupted tests on RN0.1 specimens using acoustic emission analysis. (*a*) Fracture surface after subsequent fatigue crack propagation ($T = -30$ °C) Some EBSD indexations of "crack arresting" boundaries are given. (*b*) EBSD map of a polished cross section ($T = 20$ °C). Thin lines and thick lines denote low-angle and high-angle boundaries, respectively. (*c*) Scanning electron micrograph and disorientation analysis along the crack path, showing microcrack arrest at high-angle boundaries (same area as b).

of both elongated and blocky M-A particles (as high as in the CGHAZ-120 microstructure), the obtained refined microstructure exhibited a high ductility, with a transition temperature of −150 °C for the RN2 specimens, *i.e.*, 30 °C and 60 °C lower than those of CGHAZ-25 and ICCGHAZ-25, respectively. Numerous dimples were observed on fracture surfaces of the refined bainite specimens, both within the cleavage facets and as ductile ligaments between cleavage fractured areas. This refined bainite matrix was found to hinder the propagation of cracks initiated from M-A constituents. The micromechanical model proposed in the last part of Section IV is an attempt to take into account this "double barrier" (DB) phenomenon evidenced for cleavage cracking in the simulated HAZ microstructures.

## IV. MODELING

As shown experimentally, at least for temperatures higher than −170 °C, cleavage fracture is controlled by the propagation of cleavage microcracks. The resistance to cleavage cracking is, thus, controlled by the various microstructural barriers to cleavage crack propagation. In this study, three probabilistic models accounting for propagation-controlled cleavage fracture were used. Before going into details for each of the models used, it is useful to briefly review the historical development of the so-called "local approach to brittle fracture."

The first model developed in the spirit of a local approach to fracture is the RKR model proposed by Richie *et al.*,[27] which predicts that cleavage fracture of mild steels occurs once a critical stress value is achieved over a characteristic distance. The physical meaning of this distance is not easy to clarify, even in the case of brittle M-A constituents in CGHAZ and ICCGHAZ microstructures.[28] The RKR model was then improved by introducing a size distribution of the cleavage-nucleating brittle particles, accounting for a statistical competition between (numerous) small particles and (less numerous) coarse particles in the stress field acting in front of a notch or of a crack.[29] However, multiple fracture events were supposed to occur along the crack front before final fracture. The Curry and Knott model[29] is, therefore, not a weakest-link model.

By using the (Hutchinson, Rice, and Rosengren (HRR) analytical stress and strain distribution ahead of a crack,[30,31] Curry showed that given the hardening exponent $n$ (which ranges between 0.105 and 0.14 for the simulated HAZ microstructures), the fracture toughness could be expressed as follows after Reference 32:

$$K_{Ic} = S^{-\frac{1+n}{2n}} \cdot X_0^{1/2} \cdot \sigma_f^{\frac{1+n}{2n}} \cdot \sigma_y^{-\frac{1-n}{2n}} \qquad [3]$$

where $X_0$ is the characteristic distance, $\sigma_y$ is the yield stress, $\sigma_f$ is the critical cleavage fracture stress, and $S$ is the amplitude of the singularity of the HRR stress field near the crack tip; $\sigma_0$ and $\varepsilon_0$ are material constants. Equation [3] shows that $K_{Ic}$ depends on temperature through $\sigma_y$. However, this model is not probabilistic in nature.

Several weakest-link models have been developed during the last 20 years. To account for the experimental scatter, three of them have been used, and the results are given subsequently.

### A. *Results Given by the Beremin Model*

The model developed by the Beremin group[23] was successfully used by Tagawa *et al.*[33] for HAZ microstructures containing M-A constituents. As some plastic strain is necessary for cleavage to occur, the process zone (PZ) is taken to be the plastic zone (in practice, a threshold of $\varepsilon_p = 10^{-6}$ is assumed in the present study; the exact value does not affect the results

as long as it remains very small). Concerning fracture probability, the PZ is divided into $N$ independent units having the same volume ($V_0$). The value of $V_0$ must be high enough to contain a cleavage crack initiator with a reasonable probability and low enough to allow one to neglect the stress gradients within $V_0$. Here, $V_0$ was taken to contain about eight prior austenite grains, *i.e.*, $V_0 = (100\ \mu m)^3$. In every unit of volume $V_0$, the size distribution density of defects (where cleavage microcracks initiate) is represented using a power law:

$$p(a) = \alpha \cdot a^{-\beta} \qquad [4]$$

where $a$ is the defect size and $\alpha$ and $\beta$ are $V_0$-dependent material constants. Assuming a Griffith-like criterion, the probability for a given elementary unit to fracture under maximum principal stress ($\sigma$) is then given by

$$P(\sigma) = \int_{a_c(\sigma)}^{+\infty} p(a)\, da,$$

$$\text{with } a_c(\sigma) = \frac{\pi \cdot E \cdot \gamma}{2 \cdot (1 - \nu^2) \cdot \sigma^2} \text{ (Griffith-like criterion)} \qquad [5]$$

In Eq. [5], $E$ is the Young's modulus, $\nu$ is the Poisson ratio, and $\gamma$ is the surface energy of the material. When integrating Eq. [5] using Eq. [4] for $p(a)$, one obtains the following equations for every elementary unit:

$$P(\sigma) = \left(\frac{\sigma}{\sigma_u}\right)^m \text{ with } m = 2\beta - 2 \text{ and}$$

$$\sigma_u = \left(\frac{m}{2\alpha}\right)^{1/m} \sqrt{\frac{2}{\pi} \frac{E\gamma}{1 - \nu^2}} \text{ (in plane-strain conditions)} \qquad [6]$$

Here again, $\gamma$ is the surface energy, $E$ is the Young's modulus, and $\nu$ is the Poisson ratio of the material; $\alpha$ and $\beta$ are the same material parameters as in Eq. [4]. In a 3-D structure, spatial integration over the PZ and weakest-link assumption give the following expression, provided that each individual probability ($P(\sigma)$) remains small:[23]

$$P_f = 1 - \exp\left(-\left(\frac{\sigma_w}{\sigma_u}\right)^m\right) \text{ with } \sigma_w = \left(\int_{PZ} \sigma_I^m \frac{dV}{V_0}\right)^{1/m} \qquad [7]$$

In Eq. [7], $\sigma_I$ is the local maximum principal stress given by, *e.g.*, FE calculations; and $\sigma_w$ is termed the Weibull stress. For a fixed $V_0$, two parameters have to be fitted, namely, $m$ and $\sigma_u$. It is emphasized that in Eq. [7], the specimen geometry and plastic constraint effect are taken into account through the calculation of the local stress field $\sigma_I$ (and, thus, of $\sigma_w$). The Weibull parameter ($m$) is linked to the Weibull stress and not to macroscopic loading parameters such as $K_I$ or the $J$ integral. In fact, the relationship between fracture toughness (for some fixed value of $P_f$) and specimen geometry is not obvious in the general case.

As an example application of the more general Beremin model, the effects of specimen thickness and test temperature on the fracture probability ($P_f$) can be analytically estimated under predominantly small-scale yielding conditions (*i.e.*, providing that the HRR stress field accurately describes the stress and strain fields near the crack tip) and without any stable ductile crack growth preceding unstable brittle fracture (*i.e.*, for a stationary crack). In plane-strain conditions, this leads to the following equation:

$$P_f = 1 - \exp\left(-\frac{\sigma_y^{m-4}\, B K_1^4\, C_{m,n}}{\sigma_u^m\, V_0}\right) \qquad [8]$$

Here, $\sigma_y$ is the yield stress and $C_{m,n}$ is an elliptic integral depending both on $m$ (the Weibull shape factor), on $n$ (the strain-hardening exponent), and on the two-dimensional plastic zone size. The parameter $B$ is the thickness of the specimen, and $K_I$ is the stress intensity factor. The "size" effect (here, thickness effect) is given by the fact that in plane-strain conditions, the product $K_{Ic}^4\, B$ is constant. In plane-strain conditions, the effect of temperature is driven by the yield stress as follows:

$$K_{IC}\, (\sigma_y)^{(m/4)-1} = \text{constant} \qquad [9]$$

A first estimate of $m$ was obtained by comparing Eqs. [3] and [9] (both assuming plane-strain conditions), giving $m = 2(1/n + 1) = 16$ to 21 for the simulated HAZ microstructures. Consequently, only the values of ($m$, $\sigma_u$) leading to $m \approx 20$ were accepted in the fitting procedure.

The fitted values of $m$ and $\sigma_u$ are given in Table III for all microstructures. They were fitted by using elastic-plastic FE calculations of the RN5, RN2, and RN1 specimens (all geometries and various test temperatures in the brittle temperature range),[34] followed by postprocessing calculation of both $\sigma_w$ and $P_f$. The experimental values of $P_f(\sigma_w)$ were calculated using $P_f = (i - 0.5)/N$, where $i$ is the rank of the experimental value and $N$ is the total number of tests. These experimental values were compared to those calculated from Eq. [7]. Good agreement was found between $P_f$ *vs* $\sigma_w$ curves obtained using Eq. [7] and FE calculations (Figure 9), although agreement was less good for the CGHAZ-120 microstructure. It can be noticed that with increasing $\Delta t^{8/5}$, both the yield strength and critical stress ($\sigma_u$) decrease, leading to no significant change in toughness, as was observed experimentally.

The model was then applied to the fracture toughness (TPB) specimens. Model predictions were in good agreement

**Table III. Parameters of the Beremin Model (Unit Volume $V_0 = (100\ \mu m)^3$) and of the "Master Curve" Approach for the Investigated Microstructures; $T_{100}$ is the Temperature for which $K_{Ic} = 100\ MPa\sqrt{m}$**

| Microstructure | Beremin Model | | Master Curve Approach: Fitted Value of $T_0$ (°C) | Experimental Values | |
|---|---|---|---|---|---|
| | $\sigma_u$ (MPa) | $m$ | | $T_{28J}$ (°C) | $T_{100}$ (°C) |
| Base metal | 2158 | 27 | −130 | −100 | −140 |
| CGHAZ-25 | 2670 | 20 | −45 | −40 | −55 |
| ICCGHAZ-25 | 2351 | 20 | −12 | −15 | −20 |
| CGHAZ-120 | 2085 | 20 | −6 | −15 | −10 |

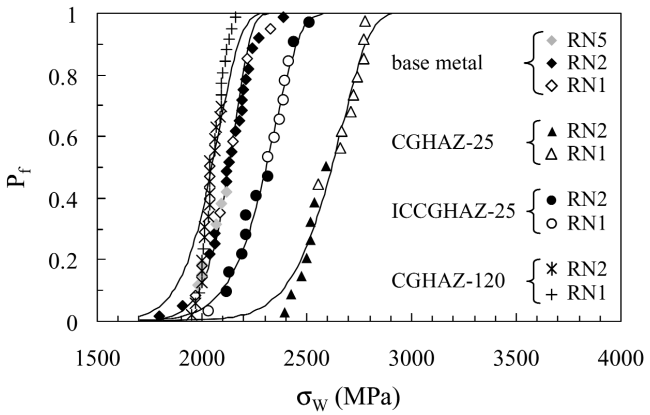


Fig. 9—Fitting results of the Beremin model to the experimental data obtained with RN specimens. $P_f$ is the fracture probability, and $\sigma_w$ is the Weibull stress.

with experimental results (Figure 5) for the simulated HAZ microstructures. Less-good agreement obtained with the base metal was attributed to the sensitivity of the model to the constitutive equations. In fact, the way of taking into account the pronounced Lüders' plateau exhibited by the base metal may influence the results given by the model.[19]

The Beremin model makes use of the fitted Weibull shape factor. In the present study, $m = 20$ to 27, whereas smaller values were found for $m$ (10 to 18) by Tagawa *et al.*[33] using the Beremin model for low-carbon steel HAZ microstructures. The values found in the present study are more typical for steels (including bainitic steels) and better agree with values deduced from Eq. [3]. However, from a theoretical point of view, the value of the parameter $m$ should be related to the defect size power-law distribution ($p(a)$) by Eq. [6]. Here, use of experimental values for $\beta$ would give $m = 5$. Thus, the Weibull slope cannot be simply related to the defect size distribution. This probably arises from the fact that cleavage crack propagation actually occurs in several steps, as shown experimentally. Moreover, AE monitoring showed that damage continuously appears during the tests, whereas the Beremin model concentrates on a distribution of already-existing defects.

### B. *Use of the Master-Curve Model*

#### 1. *Results given by the model*

In the Wallin, Saario, and Törrönen (WST) model,[35] the critical radius value ($r_0$) for a brittle particle to be broken under a given opening stress is defined using a Griffith-like, temperature-dependent criterion. The defect size distribution is different from that taken by Beremin. The fracture PZ is again divided into $N$ independent units. By assuming a random distribution of defects and provided that the individual fracture probability ($P(\sigma)$) remains small for every unit, integration over all individual volumes constituting the PZ gives the following equation:[36]

$$P_f = 1 - \exp\left(-\frac{B}{B_0}\left(\frac{K_I - K_{min}}{K_0 - K_{min}}\right)^4\right) \qquad [10]$$

Unlike in the Beremin model, a threshold value for fracture toughness ($K_{min}$) is introduced in the MC model. The parameter $K_{min}$ is related to the threshold effect induced, for instance, by the fatigue precracking procedure. The parameter $B_0$ is a normalizing constant, whereas $K_0$ is temperature dependent; it can be derived from the median value of $K_I$ ($K_{med}$) by using $K_{med} \approx 1.1\ K_0$.[36] In the MC approach, a simple empirical equation is proposed for $K_{med}$:[37]

$$K_{med}\ (B = 25\ \text{mm}) = 30 + 70 \exp\left(0.019 \cdot (T - T_0)\right)$$
$$(T \text{ and } T_0 \text{ in degree Celsius, and } K \text{ in MPa}\sqrt{\text{m}}) \qquad [11]$$

As in Reference 36, $K_{min}$ was taken to be 20 MPa$\sqrt{\text{m}}$. The temperature $T_0$ is that for which $K_{med} = 100$ MPa$\sqrt{\text{m}}$. It is usually determined using the ASTM standard E1921-97[38] using either fracture toughness data or impact toughness DBT curves.

In the present study, the fracture toughness results were converted into "1$T$" ($B = 25$ mm) values using the size effect of Eq. [10]. Then, the large-scale yielding correction proposed by Reference 36 was applied when necessary. The values of $K_{med}$ and $T_0$ were then derived. Except for the base metal, good agreement was found between the MC approach and the experimental fracture toughness results as a function of temperature (Figure 5). Less-satisfactory agreement was obtained with the base metal due to the $K_{min}$ threshold effect. In fact, some experimental values were even lower than the threshold value of 20 MPa$\sqrt{\text{m}}$ mentioned previously.

Impact toughness properties of the various HAZ microstructures[19] can also be used to derive a value for the $T_0$ temperature parameter.[38,39] Following the ASTM 1921-97 standard,[38] the value of $T_0$ should be equal to $T_{28J} + C(B)$, where $T_{28J}$ is the DBT temperature corresponding to a Charpy energy of 28 J. The value of $C(B)$ should be equal to $-32$ °C for the specimen thickness used in the present study. However, for the simulated HAZ microstructures, the corresponding values of $T_0$ are too low by about 30 °C, leading to poor agreement with experimental scatter results. This is not due to microstructure heterogeneity in the specimen (as could have been the case in actual welded joints), because the crack always propagated straight ahead, in the midplane of the Charpy or TPB specimen, *i.e.*, well within the area where the simulated HAZ heat treatment yielded the desired microstructure. Thus, for the simulated HAZ microstructures investigated here, $T_0$ had to be chosen close to $T_{28J}$, as indicated in Table III.

#### 2. *Comparison between the Beremin and MC models*

Similarities and differences between the MC approach and the Beremin model can be underlined by considering the size effect (which is the same in both models in plane-strain conditions only) and the temperature dependence of fracture toughness. In the MC approach, the temperature dependence is introduced through $K_0(T)$ or $K_{med}(T)$. If $K_{min}$ is much smaller than $K_I$ and $K_0$, both models lead to similar results if $(\sigma_y)^{(m/4)-1}$ and $K_0$ show the same temperature dependence. To check for this, the ratio of $(\sigma_y)^{(m/4)-1}$ over $K_0$ was calculated as a function of temperature. It was found that for $K_I$ and $K_0$ values much higher than $K_{min}$ (*i.e.*, $T > -150$ °C for the base metal and $T > -100$ °C for the HAZ microstructures), this ratio varies by less than 20 pct, showing that in this particular case, both the Beremin model and the MC approach are similar. However, the two approaches lead to very different results as long as the plane-strain

condition is no longer fulfilled. The MC model has to include corrections to take into account the constraint effects. The Beremin model takes the effect of specimen geometry directly into account, as long as the stress field near the crack tip is accurately determined (including constraint effects), so that the Weibull parameters $m$ and $\sigma_u$ only depend on the material and fracture micromechanism.[40,41]

Agreement between experimental results and both the Beremin and MC model predictions is fully satisfactory in the temperature range corresponding to brittle cleavage fracture. However, limitations of these models must not be neglected. The MC approach has little physical basis, in particular in the estimation of $K_0(T)$, and no way is given to the metallurgist to improve toughness properties of steels.

In the Beremin model, the value of the shape parameter, $m$, results from a fitting procedure and does not correspond to the experimental size distribution of defects. Both models assume a one-step cleavage propagation mechanism, which is not observed experimentally in the simulated HAZ microstructures. This is why a DB model, taking into account the observed influence of both M-A constituents and bainitic packet boundaries and involving continuous damage initiation, is presented in the next section.

### C. *Results given by the DB model*

The DB model was adapted from the theory developed by Martin–Meizoso *et al.*,[42] which is a probabilistic, weakest-link model for cleavage cracking of carbide-containing bainitic steels. In the present case, the brittle particles are the M-A constituents, and the bainitic microstructure is represented using the crystallographic packets investigated with EBSD. As in the Beremin and MC models, the process zone is the plastic zone (PZ). In the DB model, a critical crack initiation stress is added to the local yield criterion used in the Beremin model. Consistent with experimental observations, defects are not supposed to exist before fracture occurs.

According to the DB model, cleavage fracture occurs by following three steps successively, as depicted in Figure 10 (where, for the sake of simplicity, the crack was assumed to nucleate from an intragranular M-A constituent).

Step 0: A crack initiates at (or near) M-A constituents, by either particle/matrix interface decohesion or brittle fracture of the M-A particle. In the present case, and in order to accurately model the fracture micromechanisms observed with TPB specimens, the crack is assumed to initiate from brittle fracture of a M-A component under the critical stress $\sigma^c_{M\text{-}A}$ in the M-A particle.

Step 1: The microcrack immediately reaches the particle/matrix interface (Figure 10(b)), *i.e.*, the M-A/bainite phase boundary, of strength $\sigma_{pm}$.

Step 2: This microcrack propagates into the matrix across the particle/matrix interface and reaches the first "strong" matrix/matrix interface (Figure 10(c)), *i.e.* the first high-angle packet boundary, of strength $\sigma_{mm}$.

Step 3: The microcrack propagates across the matrix/matrix interface (Figure 10(d)), leading to final failure.

Using the weakest-link assumption, the fracture probability ($P_f$) of the specimen is then given by the combined conditional probabilities of these three events to successively occur at the same location of the specimen. Following Reference 43, $\sigma_{mm}$ is lowest at low temperatures but is assumed to increase with temperature[44] and becomes higher than $\sigma_{pm}$. If $\sigma_y$ is the yield stress of the material and $\sigma_I$ (or, respectively, $\sigma_{M\text{-}A}$) is the local maximum principal stress (or, respectively, the maximum stress in the M-A particle as given by Eq. [2]), the effect of temperature on the failure micromechanism

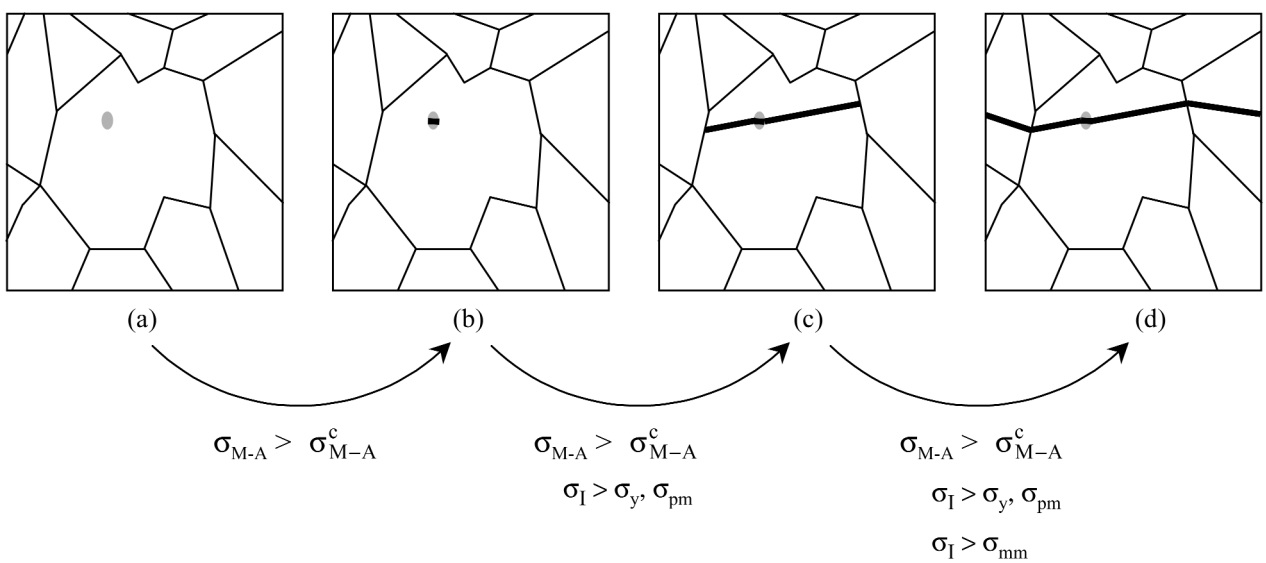


Fig. 10—Schematic representation of the role of microstructural barriers on failure micromechanisms. For the sake of simplicity, the crack was assumed to nucleate from an intragranular M-A constituent: (*a*) undamaged material, (*b*) microcrack initiation (step 0) and propagation (step 1) in the M-A particle, (*c*) microcrack propagation across the particle/matrix interface of strength $\sigma_{pm}$ (step 2), and (*d*) microcrack propagation across a bainite high-angle packet boundary of strength $\sigma_{mm}$ (step 3), leading to final failure. $\sigma_I$ is the local maximum principal stress, and $\sigma_{M\text{-}A}$ is the stress in the M-A particle, of critical value $\sigma^c_{M\text{-}A}$.

can be described by considering four temperature ranges as follows.

1. At very low temperatures (temperature range I), $\sigma_{mm} < \sigma_{pm} < \sigma_y$. As soon as $\sigma_I \geq \sigma_y$ (at least locally), the first particle-cracking event ($\sigma_{M\text{-}A} > \sigma^c_{M\text{-}A}$) immediately leads to final failure, because the local value of $\sigma_I$ is already higher than $\sigma_y$ and higher than the strength of all microstructural barriers ($\sigma_{pm}$ and $\sigma_{mm}$). Thus, in temperature range I, fracture is nucleation controlled. This is in agreement with experimental data, as no damage was observed for $T \leq -170$ °C on simulated HAZ microstructures.
2. At somewhat higher temperatures (temperature range II), $\sigma_{mm} < \sigma_{pm}$, but now $\sigma_y < \sigma_{pm}$. Upon loading, $\sigma_I$ increases, so that $\sigma_y < \sigma_I < \sigma_{pm}$, and as soon as $\sigma_{M\text{-}A} > \sigma^c_{M\text{-}A}$, microcracks initiate at particles and stop at the particle/matrix boundary. As soon as $\sigma_I$ is locally higher than $\sigma_{pm}$, a microcrack propagates into the bainitic matrix across the particle/matrix interface. At this stage, and for this microcrack, $\sigma_I > \sigma_{pm} > \sigma_{mm}$. Thus, the microcrack is already able to propagate across the matrix/matrix interface ($\sigma_I > \sigma_{mm}$), leading immediately to final failure. Thus, in temperature range II, failure is controlled by the strength of the particle/matrix interfaces. Cracked particles may be observed near the fracture surface, in agreement with experiment.
3. At higher temperatures (temperature range III), the strength of the matrix/matrix interfaces is high and $\sigma_y < \sigma_{pm} < \sigma_{mm}$. Upon loading, $\sigma_I$ increases, so that microcracks initiate in particles ($\sigma_{M\text{-}A} > \sigma^c_{M\text{-}A}$), propagate through the particle/matrix interface ($\sigma_I > \sigma_{pm}$), and stop at matrix/matrix interfaces. Upon further loading, the value of $\sigma_I$ is still increasing, and, as soon as $\sigma_I > \sigma_{mm}$ (at least locally), an arrested microcrack can further propagate across the matrix/matrix interface and leads to final failure. Thus, in temperature range III, failure is controlled by the strength of matrix/matrix interfaces, *i.e.*, of high-angle bainite packet boundaries. This is consistent with experimental detection of microcrack propagation through bainite packets and of microcrack arrest at high-angle boundaries at $T \geq -60$ °C.
4. At even higher temperatures (temperature range IV), $\sigma_{mm}$ is very high, and ductile fracture (possibly initiated at M-A particles) occurs before cleavage cracking could develop into the bainitic matrix.

Temperature ranges II and III correspond to propagation-controlled cleavage cracking (in our case, for $T > -170$ °C), where cleavage microcracks were experimentally found to initiate at M-A constituents, propagate through the M-A/bainite interface, and occasionally stop at high-angle bainite packet boundaries.

The input parameters of the model are as follows.

1. The parameter $p(c)$ is the fracture probability of a M-A constituent of size $c$ (crack initiation criterion). For the sake of simplicity, it was chosen here to be a threshold function. As soon as $\sigma_{M\text{-}A} > \sigma^c_{M\text{-}A}$ (with $\sigma_{M\text{-}A}$ given locally by Eq. [2]), particle cracking occurs.
2. The parameters $f_c(c)$ and $f_g(D)$ are the size distribution functions of M-A constituents and bainitic packets, respectively. Lognormal equations were fitted to the experimental distributions as shown in Figure 2.
3. Critical sizes for cracked M-A constituents ($c^*_\sigma$, step 2) and cracked bainitic packets ($D^*_\sigma$, step 3) are assessed as a function of the maximum principal stress, assuming a Griffith-like criterion.

The Griffith-like equations are expressed as follows, with $\beta' = 1.25$ for penny-shaped microcracks:

$$c^*_\sigma = \left(\frac{\beta' \cdot K^{pm}_{Ia}}{\sigma_I}\right)^2 \quad \begin{array}{l}\text{for microcrack propagation}\\ \text{across a M-A/matrix}\\ \text{interface of toughness } K^{pm}_{Ia}\end{array} \quad [12a]$$

$$D^*_\sigma = \left(\frac{\beta' \cdot K^{mm}_{Ia}(T)}{\sigma_I}\right)^2 \quad \begin{array}{l}\text{for microcrack propagation}\\ \text{across a packet boundary}\\ \text{of toughness } K^{mm}_{Ia}\end{array} \quad [12b]$$

In Eqs. [12a] and [12b], the fracture toughness $K^{pm}_{Ia}$ (or, respectively, $K^{mm}_{Ia}$) of interfaces is used instead of the strength $\sigma_{pm}$ (or, respectively, $\sigma_{mm}$) defined before. Following a number of literature results, $K^{pm}_{Ia}$ was taken to be independent of temperature. As a first step, $K^{mm}_{Ia}$ was also taken to be independent of temperature. With this simplifying assumption, the temperature dependence of toughness arises from the temperature dependence of yield stress only, as in the Beremin model. Work is in progress to tentatively take into account the influence of temperature on $K^{mm}_{Ia}$ using, *e.g.*, the model developed by Vasiliev.[45]

Once initiated at a M-A constituent, the cleavage microcrack follows step 2 as long as its size (which is equal to the size of the cracked particle) exceeds the value of $c^*_\sigma$ (which depends on the local loading conditions). Then, step 3 is followed if both ($c > c^*_\sigma$) and ($D > D^*_\sigma$). In practice, the size of the crack nuclei is much lower than the packet size and $c^*_\sigma < D^*_\sigma$, so that the fracture probability is given by the following equations. The correlation factors $m(c)$ and $m(D)$, used in Reference 42, were assumed to be constant and were, thus, not considered in the present study. First, the probability for a microcrack of size $c$ to nucleate and to propagate across the M-A/matrix interface is given by

$$F_c(c^*_\sigma \leq c \leq D^*_\sigma) = \int_{c^*_\sigma}^{D^*_\sigma} p(c') \cdot f_c(c') \cdot dc' \quad [13]$$

Then, the probability for the crack of size $c$ to propagate across the bainite high-angle packet boundary is

$$F_g(c^*_\sigma \leq c \leq D^*_\sigma) = \int_{D^*_\sigma}^{+\infty} \left(1 - \exp\left(-N^c_V \cdot \frac{\pi D^3}{6}\right) \cdot F_c\left(c^*_\sigma \leq c \leq D^*_\sigma\right)\right) \cdot f_g(D) \cdot dD \quad [14]$$

Here, $N^c_V$ is the number of potential crack nuclei per unit volume, and $D$ is the grain (packet) size. Following the weakest-link assumption, the failure probability of the whole specimen by cleavage fracture is then given by

$$P_f = 1 - \exp\left(-\int_{PZ} N^g_V \cdot F_g(c^*_\sigma \leq c \leq D^*_\sigma) \cdot dV\right) \quad [15]$$

In Eq. [15], $N^g_V$ is the number of potential cracking grains (bainite packets) per unit volume.

The fracture probability ($p(c')$) of M-A particles of size $c'$ was taken to be

$$p(c') = 1, \text{ if the stress in the M-A particle was } \sigma_{M\text{-}A} > \sigma^c_{M\text{-}A} \text{ or } p(c') = 0, \text{ otherwise.} \quad [16]$$

The stress in the particle was calculated using Eq. [2]. The initial value of $\sigma^c_{M\text{-}A}$, which is a material parameter, was estimated using the micromechanical approach discussed before to be 2200 MPa.

With the simplifying assumptions presented here, four parameters had to be determined: $\sigma^c_{M\text{-}A}$ (the critical fracture stress of M-A particles), $K^{pm}_{Ia}$ (assumed to be the same for all microstructures), and $K^{mm}_{Ia}$ for both the CGHAZ-25 and ICCGHAZ-25 microstructures. The values of $K^{mm}_{Ia}$ differ between these microstructures, because the numerous, martensitic M-A particles located at high-angle boundaries of ICCGHAZ-25 microstructure were found to enhance cleavage crack propagation across these boundaries, thus decreasing the value of $K^{mm}_{Ia}$. All four parameters were fitted using the experimental results of tests on RN specimens (Figure 11 and Table IV). The value of $\sigma^c_{M\text{-}A}$ is close to the initial value assessed with the micromechanical approach. The value of $K^{mm}_{Ia}$ is up to 3 times higher than the values given in literature,[15,42,46] but only refers to the high-angle packet boundaries, *i.e.*, to those having the highest fracture toughness in the microstructure.

The agreement between fracture probability given by the model and experimental data for RN specimens is good for the ICCGHAZ-25 microstructure. However, agreement is less good for the CGHAZ-25 microstructure. Nevertheless, $\sigma_c$ was supposed to be the same for both microstructures, although the size distributions of second-phase particles significantly differ in CGHAZ-25 and ICCGHAZ-25 (Figure 2). The fitting procedure then leads to an overestimation of $K^{mm}_{Ia}$ in the CGHAZ-25 microstructure, whereas quantitative agreement is obtained with the ICCGHAZ microstructure.

The model was then applied to fracture toughness specimens. The evolution of fracture toughness with temperature is well represented in both the CGHAZ-25 and ICCGHAZ-25 microstructures. Quantitative agreement is obtained with the ICCGHAZ microstructure concerning fracture probability (compare the solid lines with solid symbols in Figure 12). The model well accounts for experimental scatter, which is very satisfactory, as the prediction of scatter derives directly from the experimental size distribution of second phases and bainitic packets.

The first detection of microcrack events using AE (the lowest $K$ values corresponding to open symbols in Figure 12) occurs for stress intensity factors of about 30 to 40 MPa$\sqrt{m}$. This value agrees well with the probability for a cleavage microcrack to propagate across the particle/matrix boundary (dotted lines in Figure 12). Thus, the model satisfactorily predicts both the evolution of fracture toughness with temperature and the critical stress intensity factor for the development of stable, grain-sized microcracks during the course of the test.

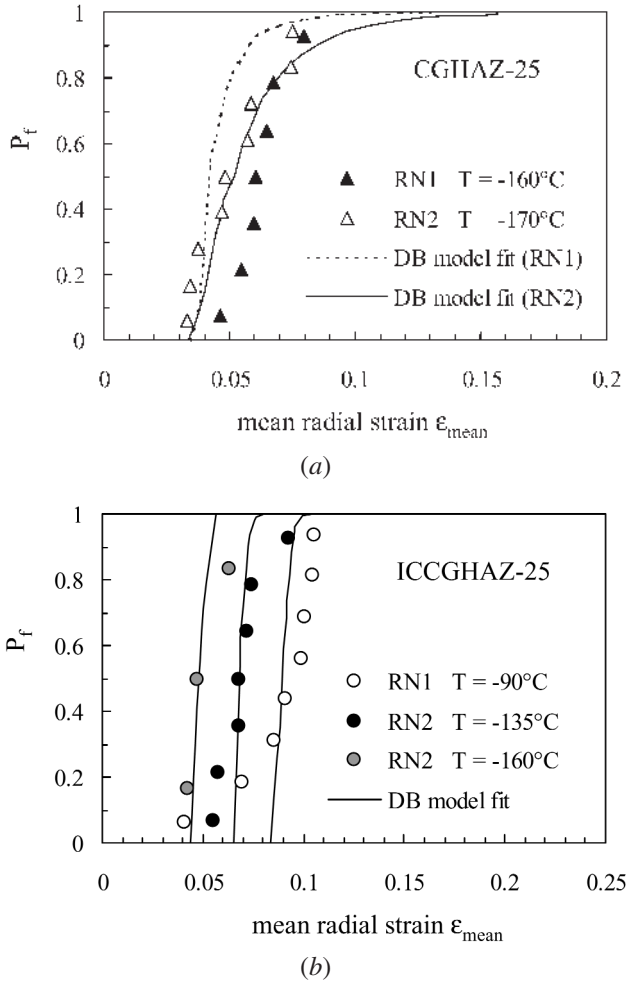


Fig. 11—Fracture probability *vs* strain—experimental data and results of fitting the "double barrier" model parameters: (*a*) CGHAZ-25 microstructure and (*b*) ICCGHAZ-25 microstructure.

**Table IV. Parameters of the "Double Barrier" Model Identified on RN Specimens, Compared with Literature Data**

| Parameter | Present Study Value | Literature Data | | |
|---|---|---|---|---|
| | | Value | Microstructural Unit | Reference |
| $\sigma^c_{M\text{-}A}$ (MPa) | 2112 | — | — | — |
| $K^{pm}_{Ia}$ (MPa$\sqrt{m}$) | 7.8 | 2.5 to 5.0 | carbides | 42 |
| | | 2.5 | globular carbides | 47 |
| | | 1.8 | TiN particles | 46 |
| $K^{mm}_{Ia}$ (MPa$\sqrt{m}$) | CGHAZ-25: | 5.0 to 7.0 | bainite packets | 15 |
| | 28 (−160 °C) | 7.0 (−196 °C) | bainite packets | 42 |
| | | 7.5 | ferrite grains | 47 |
| | ICCGHAZ-25: | 4.8 (−196 °C) | bainite packets | 46 |
| | 18 (−135 °C) | 15.2 (−50 °C) | bainite packets | 46 |

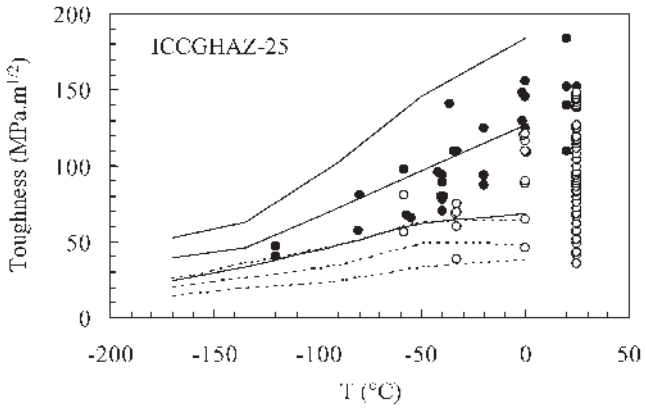


Fig. 12—Results of the double barrier model with TPB specimens. Open circles denote microcrack events; solid circles are for final fracture of the specimens. Solid (respectively, dotted) lines represent 10, 50, and 90 pct probabilities for the specimen to fracture (respectively, for a cleavage microcrack to propagate across a particle/matrix boundary) as given by the DB model.

Significant improvement of the DB model could likely be obtained by (1) separately identifying the initiation and propagation parameters, (2) refining the initiation criterion ($p(c)$), (3) adjusting the evolution of $K_{Ia}^{mm}$ with temperature, and (4) using probabilistic models for propagation across microstructural barriers.

## V. CONCLUSIONS

Experimental investigations and modeling of cleavage fracture properties of simulated HAZ microstructures of a high-strength low alloy steel led to the following results.

1. Both the M-A constituents and the coarse upper bainite microstructure have a deleterious effect on the toughness properties.
2. The fracture mechanisms of RN bars and fracture mechanics specimens are similar in nature. Thanks to original investigation techniques such as acoustic emission, the temperature range where fracture is controlled by crack nucleation (or, respectively, crack propagation) could be determined. For temperatures higher than −170 °C, cleavage fracture is controlled by the propagation of microcracks initiated near M-A constituents.
3. The damage mechanism leading to crack initiation (fracture of M-A particles *vs* decohesion from the matrix) depends on the local stress and strain state.
4. The EBSD investigations confirmed that cleavage crack propagation is controlled by the high-angle bainite packet boundaries; the number of arrested cracks increases with increasing test temperature.
5. Interrelationships between statistical models developed by Wallin (the MC model) and Beremin have been evidenced. For fracture toughness values significantly higher than the threshold value of the MC approach, but still in the brittle temperature range, both models yield to similar results in the present case.
6. For the simulated HAZ microstructures studied, the Beremin statistical model, fitted using RN specimens, is able to capture the dependence of fracture toughness upon temperature.
7. A DB model, taking into account the experimental size distribution of M-A constituents and bainitic packets, was applied to the simulated HAZ microstructures. The model satisfactorily predicts the fracture toughness values and scatter, at least for one of the simulated HAZ microstructures. The use of temperature dependent strength of high-angle packet boundaries is much more difficult and still requires further investigation.

## ACKNOWLEDGMENTS

Financial support and constant interest from Dillinger Hütte are gratefully acknowledged.

## APPENDIX

### AE Detection of Microcracking Events

As explained in more detail in Reference 21, acoustic emission was continuously recorded during the tests by

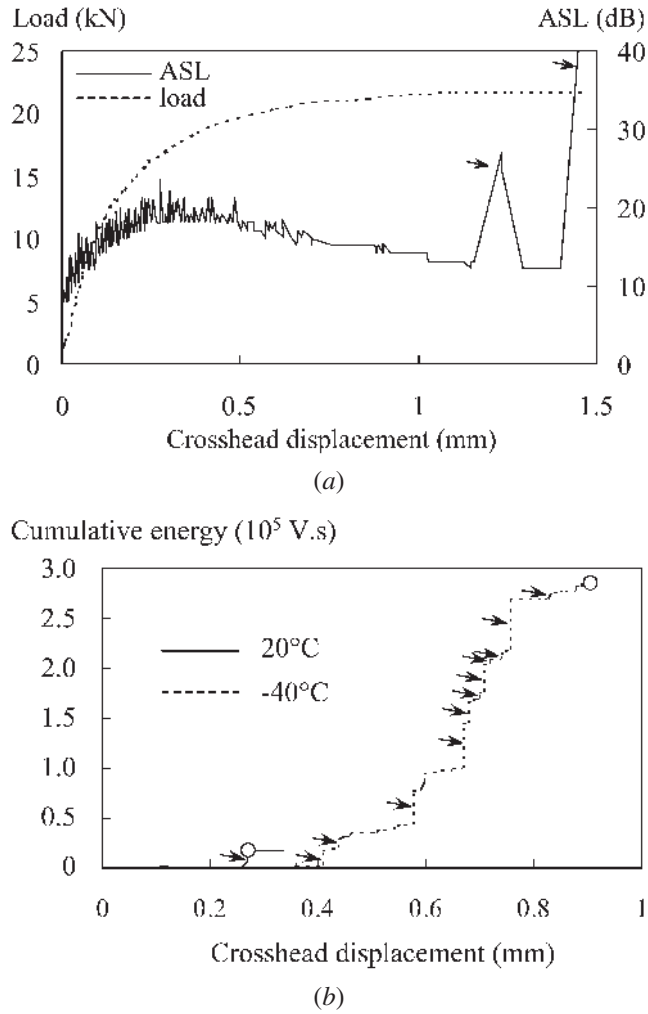


Fig. A1—Typical curves obtained with AE monitoring of microcrack propagation. (*a*) Evolution of the average signal level (ASL) and load for a RN0.1 specimen of CGHAZ-120 microstructure tested at 20 °C. (*b*) Evolution of cumulative energy with time for TPB specimens of ICCGHAZ-25 microstructure. Specimen fracture is indicated by open symbols. Energy peaks corresponding to microcrack propagation and arrest events are indicated by arrows.

means of piezoelectric sensors attached to both ends of the specimens. This technique allows both the detection and location of microcrack events. In the present study, all microcracking events were found to occur in the gage area of the specimens, *i.e.*, in the notched area. Figure A1 shows typical curves recorded during the tests.

In the beginning of the test, continuous acoustic emission is attributed to dislocation motion and possibly to phase transformation of retained austenite in the M-A constituents. The emission level is about 10 to 20 dB. Then, at low temperature, unstable fracture occurs abruptly. On the other hand, for all tests performed at −30 °C and +20 °C, and for most of the tests performed at −60 °C, unstable fracture was preceded by high-energy emission over very short times, corresponding to microcrack propagation and arrest. The emission level was much higher than the background, typically higher than 100 dB at −30 °C and −60 °C, allowing easy detection of these peaks. The resulting curves showing cumulative emission energy *vs* time are thus closely related to detection of microcrack propagation.

## REFERENCES


1. L. Devillers and D. Kaplan: Technical Report No. RE 88318, IRSID, Maizières-lès-Metz, Cedex, 1988 (in French).
2. C.L. Davis and J.E. King: *Metall. Mater. Trans. A*, 1994, vol. 25A, pp. 563-73.
3. T. Haze and S. Aihara: IIW Document No. IX-1423-86, IIW, Roissy, France, May 1986, pp. 1-38.
4. M. Toyoda: *Fracture Toughness Evaluation of Steel Welds. Review Part II*, University of Osaka, Osaka, 1988.
5. K. Okamoto, S. Aihara, A. Yoshie, T. Hasegawa, M. Kibe, H. Makino, H. Kawasaki, N. Doi, T. Tsuzuki, R. Chijiiwa, and N. Saito: *Pacrim Weldcon'92—Darwin "Transferring Technology and know-How*," Darwin, Australia, 1992.
6. K.L. Kenney, W.G. Reuter, H.S. Reemsnyder, and D.K. Matlock: *Fatigue and Fracture Mechanics*, ASTM STP 1321, J.H. Underwood, B.D. Macdonald, and M.R. Mitchell, eds., ASTM, Philadelphia, PA, 1997, vol. 28, pp. 427-49.
7. Z.L. Zhou and S.H. Lin: *Acta Metall. Sinica (English Lett.)*, 1998, vol. 11, pp. 87-92.
8. O.M. Akselsen, J.K. Solberg, and Ø. Grong: *Scand. J. Metall*., 1988, vol. 17, pp. 194-200.
9. B.C. Kim, S. Lee, N.J. Kim, and D.Y. Lee: *Metall. Trans. A*, 1991, vol. 22A, pp. 139-49.
10. F. Matsuda, K. Ikeuchi, H. Okada, I. Hrivnak, and H.S. Park: *Trans. JWRI*, 1994, vol. 23, pp. 231-38.
11. R.E. Dolby and J.F. Knott: *J. Iron Steel Inst*., 1972, vol. 210, pp. 857-65.
12. J.P. Naylor and P.R. Krahe: *Metall. Trans*., 1974, vol. 5, pp. 1699-701.
13. E. Bouyne, H.M. Flower, T.C. Lindley, and A. Pineau: *Scripta Mater*., 1998, vol. 39, pp. 295-300.
14. A.-F. Gourgues, H.M. Flower, and T.C. Lindley: *Mater. Sci. Technol*., 2000, vol. 16, pp 26-40.
15. P. Brozzo, G. Buzzichelli, A. Mascanzoni, and M. Mirabile: *Met. Sci*., 1977, vol. 11, pp. 123-29.
16. J.H. Chen, Y. Kikuta, T. Araki, M. Yoneda, and Y. Matsuda: *Acta Metall*., 1984, vol. 32, pp. 1779-88.
17. S. Aihara and T. Haze: TMS Annual Meeting, TMS, Warrendale, PA, 1988, paper no. A88-14.
18. A. Lambert, J. Drillet, A.F. Gourgues, T. Sturel, and A. Pineau: *Sci. Technol. Welding Joining*, 2000, vol. 5, pp. 168-73.
19. A. Lambert-Perlade: Ph.D. Thesis Ecole des Mines de Paris, Paris, 2001 (in French).
20. *Standard Test Method for Measurement of Fracture Toughness*, ASTM E1820-01, ASTM Standards, New York, NY, 2001.
21. A. Lambert, X. Garat, T. Sturel, A.F. Gourgues, and A. Gingell: *Scripta Mater*., 2000, vol. 43, pp. 161-66.
22. A. Pineau: in *Advances in Fracture Research (ICF5)*, D. François, ed., Pergamon Press, Oxford, United Kingdom, 1981, vol. 2, pp. 553-77.
23. F.M. Beremin: *Metall. Trans. A*, 1983, vol. 14A, pp. 2277-87.
24. R.M. McMeeking: *J. Mech. Phys. Solids*, 1977, vol. 25, pp. 357-81.
25. A. Lambert, A.-F. Gourgues, T. Sturel, and A. Pineau: *Euromat 2000*, D. Miannay, P. Coste, D. François, and A. Pineau, eds, Elsevier, Amsterdam, 2000, pp. 97-102.
26. A. Echeverría and J.M. Rodriguez-Ibabe: *Mater. Sci. Eng*., 2003, vol. A346, pp. 149-58.
27. R.O. Ritchie, J.F. Knott, and J.R. Rice: *J. Mech. Phys. Solids*, 1973, vol. 21, pp. 395-410.
28. S. Lee, B.C. Kim, and D. Kwon: *Metall. Trans. A*, 1993, vol. 24A, pp. 1133-41.
29. D.A. Curry and J.F. Knott: *Met. Sci*., 1979, vol. 13, pp. 341-45.
30. J.R. Rice and G.F. Rosengren: *J. Mech. Phys. Solids*, 1968, vol. 16, pp. 1-12.
31. J.W. Hutchinson: *J. Mech. Phys. Solids*, 1968, vol. 16, pp. 13-31.
32. D.A. Curry: *Met. Sci*., 1980, vol. 14, pp. 319-26.
33. T. Tagawa, T. Miyata, S. Aihara, and K. Okamoto: *Int. Symp. on Low-Carbon Steels for the 90's*, R. Asfahani and G. Tither, eds., TMS, Warrendale, PA, 1993, pp. 493-500.
34. F.M. Beremin: *J. Méc. Appl*., 1980, vol. 4, pp. 307-25 and 327-42 (in French).
35. K. Wallin, T. Saario, and K. Törrönen: *Met. Sci*., 1984, vol. 18, pp. 13-16.
36. K. Wallin: in *Defect Assessment in Components—Fundamentals and Applications, ESIS/EGF9*, J.G. Blauel and K.-H. Schwalbe, eds., Mechanical Engineering Publications, London, 1991, pp. 415-45.
37. K. Wallin: *Int. J. Pres. Ves. Piping*, 1993, vol. 55, pp. 61-79.
38. *Standard Test Method for Determination of Reference Temperature, $T_0$, for Ferritic Steels in the Transition Range*, ASTM E1921-97, ASTM Standards, New York, NY, 1997, pp. 1068-84.
39. G. Sanz: *Rev. Metall., Cah. Inf. Tech*., 1980, vol. 77, pp. 621-42.
40. F. Minami, A. Brückner-Foit, D. Muntz, and B. Trolldenier: *Int. J. Fract*., 1992, vol. 54, pp. 197-210.
41. K. Hojo, I. Muroya, and A. Brückner-Foit: *Nucl. Eng. Des*., 1997, vol. 174, pp. 247-58.
42. A. Martín-Meizoso, I. Ocaña-Arizcorreta, J. Gil-Sevillano, and M. Fuentes-Pérez: *Acta Metall. Mater*., 1994, vol. 42, pp. 2057-68.
43. T. Lin, A.G. Evans, and R.O. Ritchie: *Metall. Trans. A*, 1987, vol. 18A, pp. 641-51.
44. T. Narström and M. Isacsson: *Mater. Sci. Eng*., 1999, vol. A271, pp. 224-31.
45. A. Vasilev, S. Firstov, and A. Koval: in *Recent Advances in Fracture*, R.K. Mahidhara, A.B. Geltmacher, P. Matic, and K. Sadananda, eds., TMS, Warrendale, PA, 1997, pp. 315-26.
46. J.M. Rodrigues-Ibabe: *Mater. Sci. Forum*, 1998, vols. 284–286, pp. 51-62.
47. G.T. Hahn: *Metall. Trans. A*, 1984, vol. 15A, pp. 947-59.